




# Controlling spin-polarized carriers at the SrTiO<sub>3</sub>/EuO interface via the ferroelectric field effect

Wente Li , Lingyuan Gao , and Alexander A. Demkov <sup>\*</sup>

*Department of Physics, The University of Texas, Austin, Texas 78712, USA*



(Received 15 April 2020; accepted 29 June 2020; published 27 July 2020)

Using density functional theory and phenomenological Landau-Khalatnikov theory, we investigate the effect of spontaneous polarization switching in BaTiO<sub>3</sub> on the oxygen vacancy-induced electron gas at the adjacent SrTiO<sub>3</sub>/EuO interface in epitaxial BaTiO<sub>3</sub>/SrTiO<sub>3</sub>/EuO heterostructures. The ferroelectric field effect, induced by BaTiO<sub>3</sub> (BTO) in oxygen-deficient SrTiO<sub>3</sub> (STO) in the presence of a ferromagnetic semiconductor EuO, results in a spin-polarized carrier gas at the interface due to the magnetoelectric proximity effect.

DOI: [10.1103/PhysRevB.102.035308](https://doi.org/10.1103/PhysRevB.102.035308)

## I. INTRODUCTION

Following the discovery of the conducting interfacial layer between two large-band gap insulators LaAlO<sub>3</sub> (LAO) and SrTiO<sub>3</sub> (STO) by Ohtomo and Hwang [1], transition metal oxide heterostructures have attracted tremendous interest. LAO is a polar oxide with positively charged LaO layers alternating with negatively charged AlO<sub>2</sub> layers along the [001] direction. STO, on the other hand, is a paraelectric perovskite with charge-neutral TiO<sub>2</sub> and SrO layers stacked along [001]. Further research has demonstrated that the two-dimensional electron gas (2DEG) near the LAO-STO interface exhibits complex and interesting properties, including para- and ferromagnetism that, surprisingly, can coexist with superconductivity [2]. The microscopic mechanism of the formation of the 2DEG is still debated. One explanation suggests a “polar catastrophe” [3,4], meaning that the electrons from the LAO surface are transferred to the LAO-STO interface to prevent the electrostatic potential from diverging. Another explanation [5,6] is that the 2DEG stems from oxygen vacancies in STO generated during growth. The oxygen vacancy (OV) is a common defect in crystalline oxide films grown under reducing environments such as that in molecular-beam epitaxy (MBE). It has a profound effect on the properties of transition metal oxide interfaces [7,8]. In STO, the OV is a donor [9] and, therefore, it can contribute carriers to the 2DEG. It also produces an in-gap state that can be detected by angle-resolved photoemission spectroscopy [10]. There have been many reports of vacancy-induced carriers at many oxide interfaces [7,10–12].

As continuing Moore’s law scaling has become more challenging over the last two decades, the search for new means of information processing has intensified. Spintronic devices, where operation is based on a highly spin-polarized 2DEG, provides one possible way. The formation of a spin-polarized 2DEG at the interfaces of oxides, such as LAO/BaTiO<sub>3</sub> [13], SrMnO<sub>3</sub>/LaMnO<sub>3</sub> [14], and several EuO-related structures [10,15–19], has been the focus of active research. Interesting 2DEG phenomena have been reported for

heterostructures with EuTiO<sub>3</sub> [26–28] that bear some similarities to the STO/EuO system. One of the best-known spintronic devices, a spin field effect transistor (spin FET), was suggested by Datta and Das [20]. In a spin FET, the spin injection efficiency at the ferromagnetic metal/semiconductor junction is limited by the conductivity mismatch between the two materials [21–23]. To address this issue, other more complicated structures using ferromagnetic (FM) semiconductors have been proposed [21,24,25].

EuO is one such ferromagnetic semiconductor that could be used to generate the spin-polarized 2DEG in these spin metal–oxide–semiconductor field-effect transistors (MOSFETs). Below its Curie temperature of 69 K, EuO becomes ferromagnetic and shows a large  $\sim 0.5$  eV spin splitting in the conduction band that, upon doping, could result in a 100% spin-polarized 2DEG, if the carriers resided at the EuO side of the interface. In addition, doped EuO would have a slightly higher Curie temperature [16], potentially exceeding that of liquid nitrogen, thus making EuO very attractive in applications. Unfortunately, in the case of the STO/EuO heterostructure, it was found that due to the inherent band alignment at the interface, the carriers reside mostly at the STO side [10,15]. Thus, finding a way of controlling the location of carriers in the STO/EuO heterostructure is key to realizing this interesting functionality.

Fredrickson and Demkov have recently discussed a switchable conductivity at the BaTiO<sub>3</sub> (BTO)/STO interface; they found that the charge density was controlled by the direction of ferroelectric polarization of the BTO layer [29]. Here, we explore how this mechanism may control the 2DEG at the interface of EuO and oxygen-deficient STO in proximity to a ferroelectric by studying the BTO/STO/EuO heterostructure using density functional theory (DFT). We demonstrate that when STO is oxygen deficient, one can indeed move the 2DEG from STO to EuO by switching the direction of polarization in BTO and, thus, achieve EuO doping. A similar ferroelectric field effect was demonstrated for the BTO/STO/Ge heterostructure (with the difference being that Ge was doped *n* type) [30]. The rest of the paper is organized as follows. We briefly introduce the computational methodology and analysis tools used here in Sec. II. In Sec. III, we present the results and discuss the field effect with and without an oxygen vacancy. In

<sup>\*</sup>demkov@physics.utexas.edu

Sec. III C, we discuss the polarization distribution across the perovskite layers using the mesoscopic Landau-Khalatnikov theory and compare it with first-principles calculations. We summarize our results in Sec. IV.

## II. COMPUTATIONAL METHODOLOGY

We use DFT as implemented in the Vienna *Ab-initio* Simulation Package (VASP) [31]. The generalized gradient approximation (GGA) [32] and projector-augmented-wave (PAW) potentials [33] are employed. We use the valence configurations  $5s^25p^66s^2$  for barium (Ba),  $3p^64s^23d^2$  for titanium (Ti),  $4s^24p^65s^2$  for strontium (Sr),  $5s^25p^64f^76s^2$  for europium (Eu), and  $2s^22p^4$  for oxygen (O). In order to describe the correlated  $4f$  states of Eu and  $3d$  states of Ti, we use the Hubbard  $U$  correction (GGA+ $U$  method) with  $U = 5.0$  and  $4.36$  eV for Eu and Ti, respectively [15]. Integrals over the Brillouin zone are evaluated using Monkhorst-Pack  $k$ -point meshes ( $6 \times 6 \times 1$  for the BTO/STO/EuO heterostructure and  $8 \times 8 \times 8$  for bulk BTO, STO, and EuO). We use a cutoff energy of 600 eV to treat the heterostructure and 800 eV for bulk calculations. All heterostructures are optimized with respect to ionic positions until the forces are less than 20 meV/Å (10 meV/Å for bulk materials). The electronic step convergence at each ionic step is  $1 \times 10^{-6}$  eV for bulk materials and  $1 \times 10^{-4}$  eV for heterostructures.

In the heterostructure, STO is also envisioned as the substrate material and all other layers are strained to match its lattice constant, though the substrate is not explicitly included in the calculation. At room temperature, STO is cubic and paraelectric. The calculated lattice constant of bulk STO is 3.95 Å with the GGA+ $U$  ( $U = 4.36$  eV) method. Our result is similar to the DFT value from Ref. [15], which is slightly larger than the experimental value of 3.91 Å. The calculated STO band gap is 2.26 eV, close to that in Ref. [15], but underestimated compared to the experimental value of 3.2 eV. As discussed in Ref. [15], the choice of the  $U$  value for Ti is important, since we need to introduce an OV and the energy position of the defect level is sensitive to the value of  $U$  [9]. At room temperature, BTO is tetragonal and ferroelectric. The epitaxial growth of BTO on STO substrate results in a theoretical compressive strain of 1.96%. Also using the GGA+ $U$  method, the in-plane BTO lattice constant is  $a = 4.03$  Å and the out-of-plane lattice constant is  $c = 4.07$  Å, with a  $c/a$  ratio of 1.0099. Again, the lattice constants are slightly larger than the experimental values ( $a = 3.99$  Å,  $c = 4.03$  Å [34]), but the  $c/a$  ratio agrees well with experiment. Unfortunately, the specific implementation of the Hubbard  $U$  eliminates spontaneous polarization in BTO (due to a combination of the lattice constant, as well as electronic structure changes [35]), and renders it paraelectric (within GGA, BTO is ferroelectric). We examine the effect of  $U$  on the BTO spontaneous polarization and find that 2.7 eV is the critical  $U$  value to stabilize observable polarization. We will discuss the choice of  $U$  in more detail in the following paragraphs. The optimized lattice constant of bulk EuO is 5.19 Å, which agrees well with the previous theoretical result [15,36] and the experimental value of 5.14 Å. EuO experiences a theoretical +7.74% tensile strain when matched to STO [37]. The EuO band gap between the spin-up Eu  $4f$  and  $5d$  states is 1.17 eV,

in good agreement with the experimental value of 1.12 eV and previous calculations [15,36].

When investigating the heterostructure, we use the simulation cells shown in Fig. 1. We define a one-unit cell of perovskite BTO or STO as a cell between two  $\text{TiO}_2$  layers [as shown in Fig. 1(a)]. Hence, on the left-hand side, the simulation cell is comprised of an eight-unit-cell-thick [Figs. 1(a) and 1(c)] or ten-unit-cell-thick [Figs. 1(b) and 1(d)]  $\text{TiO}_2$ -terminated BTO slab that is lattice matched to the assumed STO substrate on the left, followed by three-unit cells of STO. The STO is further interfaced with six layers of strained EuO. Eight- to ten-unit cells of BTO lead to a stable polarization. A three-unit-cell-thick STO layer is enough to accommodate the OV. A six-unit-cell-thick slab of EuO is found to produce the bulklike EuO electronic structure. To match the EuO rocksalt structure on perovskite STO, we rotate EuO  $45^\circ$  as shown in the inset panel of Fig. 1(a). As discussed in Ref. [15], there are two possible ways to match STO and EuO that differ in whether Eu is on top of a hollow site of the  $\text{TiO}_2$  surface (this maintains the Ti-O bond pattern of STO across the interface) or is above oxygen (this maintains the Eu-O bond pattern of EuO). Following the conclusion of Ref. [15] that the former structure is more stable, we limit our consideration to the hollow site match. The simulation cell has 14 Å of vacuum to avoid the spurious interaction between the periodic images. We use the dipole correction to make the field across the simulation cell compatible with the periodic boundary conditions. We consider two polarization states in compressively strained BTO; in one, polarization is pointing away from the BTO/STO interface ( $P_-$  configuration), and in the other, it is pointing towards the interface ( $P_+$  configuration). The direction of polarization is defined by the direction of the dipole moment of the  $\text{TiO}_2$  plane. If the Ti atom moves towards the BTO/STO interface relative to the O atoms, then it is in the  $P_+$  configuration, defined as the positive direction. Consequently, the  $P_-$  configuration is oppositely directed and negative. To examine the effects of charge introduced by an oxygen vacancy in STO, we introduce a vacancy in the subinterfacial SrO plane near the STO/EuO interface, as shown in Figs. 1(c) and 1(d), which is the lowest energy configuration [10]. As a result, we have four different heterostructures shown in Figs. 1(a)–1(d). We call them structure I ( $P_+$ , no OV), structure II ( $P_-$ , no OV), structure III ( $P_+$ , OV), and structure IV ( $P_-$ , OV). Because the different sizes of the simulation cells result in different oxygen vacancy concentrations, we test both  $\sqrt{2} \times \sqrt{2}$  and  $2 \times 2$  lateral cell sizes in order to make sure the effects induced by an OV are captured. We found that in a  $\sqrt{2} \times \sqrt{2}$  cell the OV density is too high, as we could not resolve the in-gap vacancy state shown in Fig. 2(c) of Ref. [15]. Hence, to describe the OV in STO, we use a large  $2 \times 2$  lateral supercell for structures III and IV.

It was shown in Ref. [29] that in a thin slab, polarization pointing away from the BTO/STO interface is not stable. This is because in the  $\text{TiO}_2$  plane at the BTO surface (in experiment this plane would face the STO substrate), Ti moves inward, making O the topmost layer. This creates polarization in the opposite direction compared with the  $P_-$  configuration, resulting in a domain wall near the BTO surface, which costs additional energy. In other words, if the thickness of

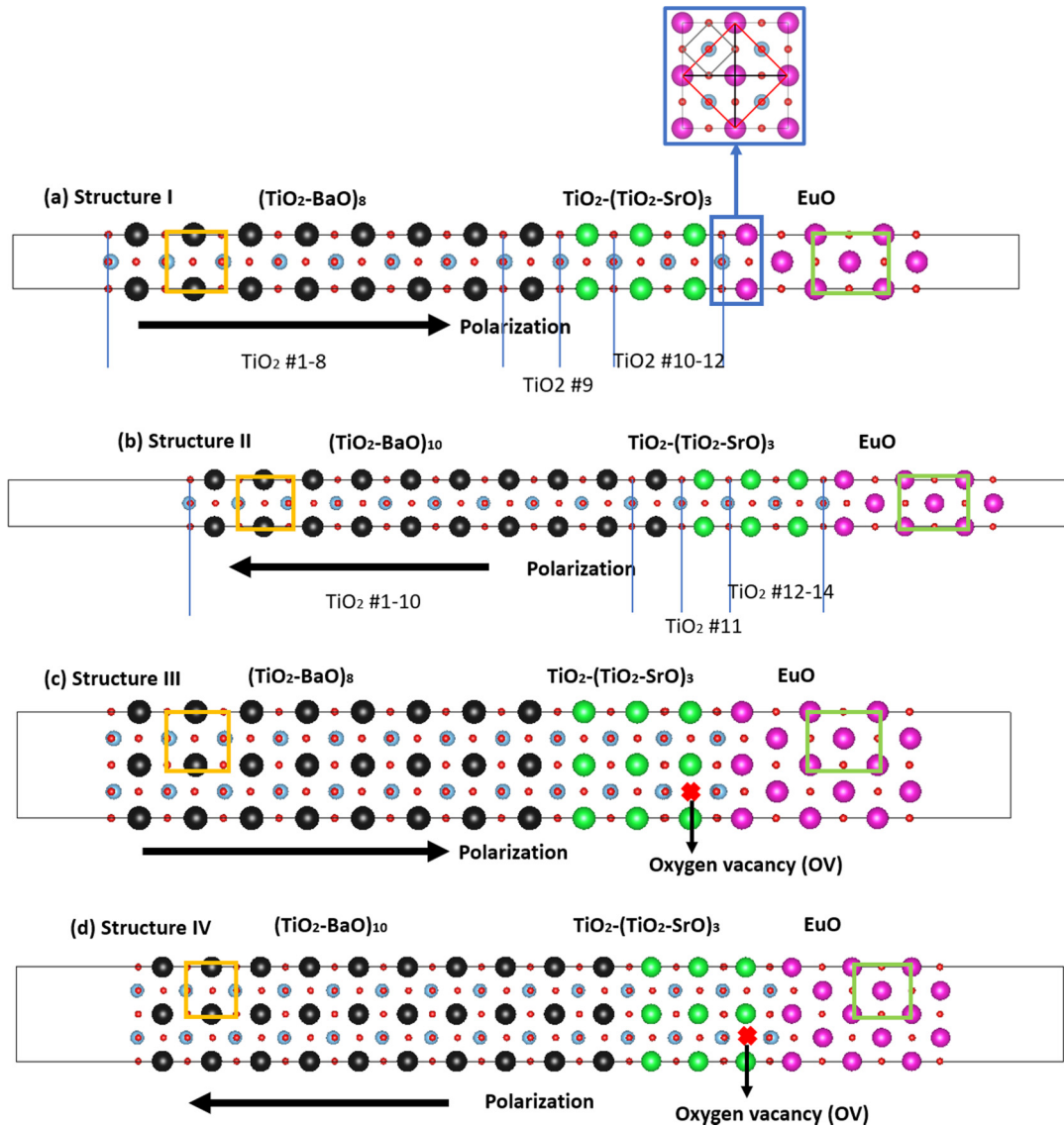


FIG. 1. (a)–(d) Four heterostructures with and without OV and two different polarization states, viewing along [100] direction. Black balls represent Ba, blue Ti, red O, and pink Eu. Yellow rectangular box represents one perovskite cell for BTO or STO and green a 45° rotated EuO rocksalt. Red crosses represent an oxygen vacancy residing in the SrO plane nearest to the STO/EuO interface. Black arrows represent two polarization directions. Inset: the details of the lattice match between EuO rocksalt and STO perovskite, indicated by a blue box at the STO/EuO interface. Red square represents conventional EuO rocksalt cell (top view). The grey square is top view of the  $\text{TiO}_6$  octahedron. The angle between black and red squares is 45°. This interface structures applies to all four interfaces.

BTO is comparable with the thickness of the domain wall, theoretically, the  $P_-$  configuration cannot be stabilized and BTO relaxes to a paraelectric phase. As a result, in our calculations polarization always prefers to point towards the BTO/STO interface ( $P_+$  configuration). To stabilize the  $P_-$  configuration and achieve controllable field effect, we initially use a thicker BTO slab (12-unit cell) in structures II and IV, compared with the 8-unit-cell slab of the  $P_+$  configuration, to make sure BTO is thicker than the domain wall. We then discard the BTO layers left of the domain-wall transition region and the remaining 10-unit-cell-thick BTO slab, with the same polarization direction (pointing away from BTO/STO interface), is used, as indicated in Figs. 1(b) and 1(d).

Perhaps the most significant technical difficulty of a heterostructure calculation is the GGA+ $U$  method itself, as it

eliminates the spontaneous polarization of tetragonal BTO [29]. To circumvent this problem, we divide our calculations into three stages. First, we use pure GGA to relax the BTO/STO (Fig. 2) structure (in GGA, BTO is ferroelectric). Then, we use GGA+ $U$  and rerelease STO while keeping all BTO layers fixed to maintain polarization. Finally, we add the EuO layers and use GGA+ $U$  to relax the STO/EuO part of the simulation cell while keeping BTO fixed. As we show in the next section, the polarization profile obtained via this method agrees well with the results of the mesoscopic Landau-Khalatnikov model [38], suggesting that the approach is reasonable, though undoubtedly cumbersome.

To investigate the electronic structure of all four heterostructures, we use a combination of projected density of states (PDOS) analysis and average electrostatic potential

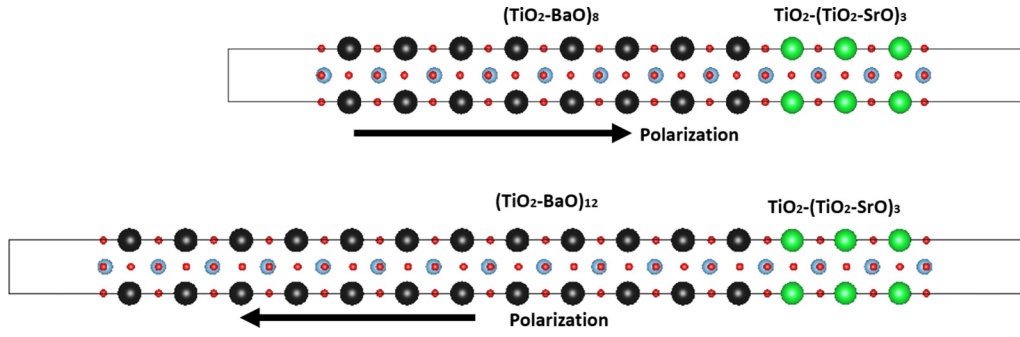


FIG. 2. Before adding six layers of EuO, to obtain the polarization states of BTO, we calculate these two BTO/STO structures (viewed along [100]), with two different polarization directions. The relaxed structures are then used to build simulation cells of Figs. 1(a)–1(d).

(AEP) method [39]. The AEP across the heterostructure is calculated using the following equation:

$$\bar{V}(z) = \frac{1}{abc} \int_{z-a/2}^{z+a/2} dz' \int_{z'-a/2}^{z'+b/2} dz'' \int_{z''-c/2}^{z''+c/2} V(z''') dz''', \quad (1)$$

where  $a$ ,  $b$ , and  $c$  are the lattice constants of EuO, STO, and BTO, respectively, and  $V(z''')$  is the local electrostatic potential. Combining these two methods, we can clearly observe the field effect induced by BTO, as well as the spin-polarized two-dimensional electron gas (2DEG) and two-dimensional

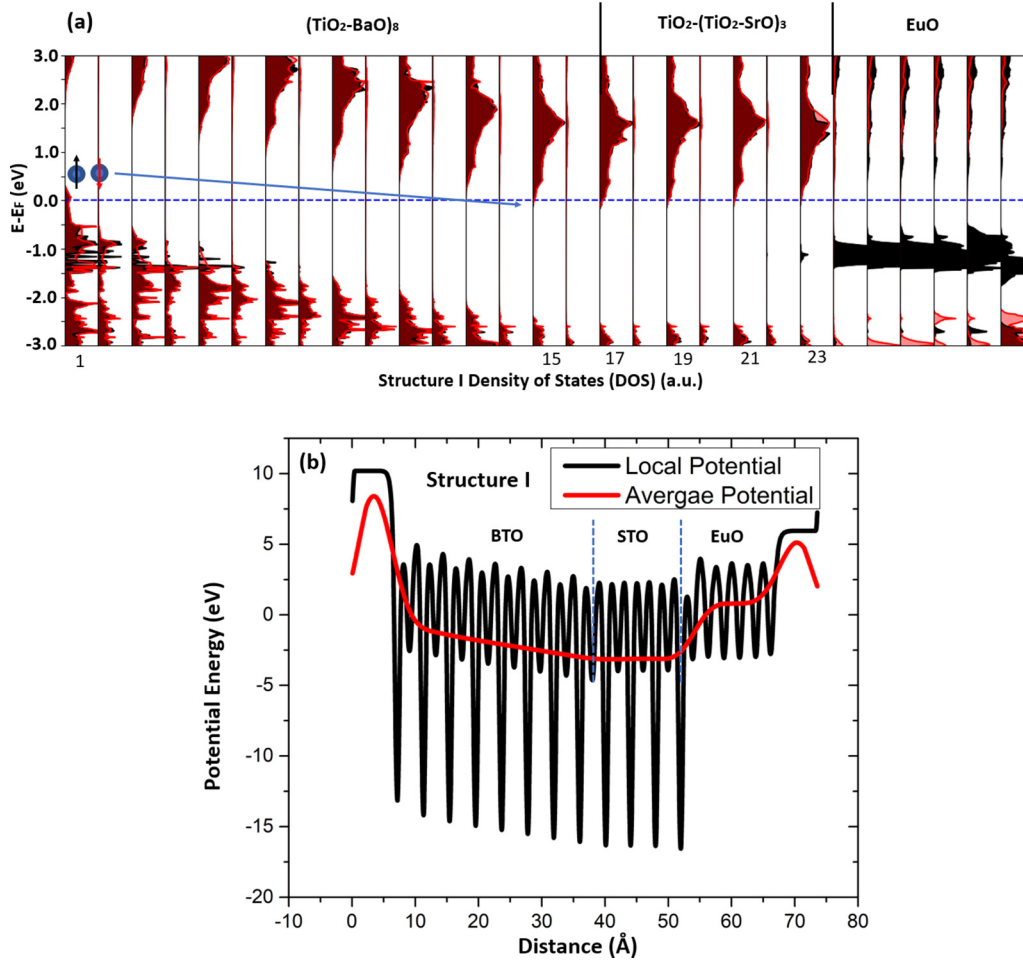


FIG. 3. (a) Projected density of states (PDOS) analysis of structure I including both spin-up and -down channel. The dark red represents the overlap between spin-up and -down channels, the light red indicates spin-down states, and black is spin-up states. The color representation applies for all the following PDOS figures. The zero energy is set at the Fermi level. The balls with black up and red down arrows represent spin-up and -down electrons and the blue arrow shows the direction of charge transfer due to the BTO field effect. (b) The local electrostatic potential (black line) and macroscopically averaged potential (red line) are plotted vs the  $z$  direction of the simulation cell. The red line is calculated from Eq. (1).



hole gas (2DHG). We will now analyze the PDOS and AEP for all four structures.

### III. RESULTS AND DISCUSSION

We will start by discussing the effect of the polarization direction on the electronic structure of the ideal, STO-strained BTO/STO/EuO heterostructure. Next, we will introduce an oxygen vacancy in the STO region, similar to what has been considered by Kormondy *et al.* [10] and Gao and Demkov [15], but with the added complexity of the ferroelectric polarization. The mesoscopic Landau-Khalatnikov model will help us gain physical insight into the polarization distribution, across the STO region.

#### A. Field effect in BaTiO<sub>3</sub>/SrTiO<sub>3</sub>/EuO heterostructure in the absence of oxygen vacancy

Figure 3 shows the layer-by-layer PDOS and AEP for structure I. The electric field across the BTO layer is clearly seen, and it is being screened in the STO and EuO layers. The electric field is pointing from the BTO/STO interface towards the BTO surface. At the BTO surface the Fermi level crosses the valence band, indicating the presence of a 2DHG, localized at the surface TiO<sub>2</sub> layer. At the BTO/STO interface, the Fermi level crosses the BTO conduction band near the interface indicating the presence of a 2DEG [shown by the blue arrow in Fig. 3(a)]. These carriers create a depolarizing field across the BTO layer to screen the ferroelectric polarization. The STO lattice also screens it, but at this thickness, the electronic screening appears to be more efficient. Computing the spin polarization as  $p = \frac{n^\uparrow - n^\downarrow}{n^\uparrow + n^\downarrow}$ , where  $n^\uparrow$  and  $n^\downarrow$  represent spin up and down electrons, we get  $p = 0$  for the 2DEG and 2DHG in all TiO<sub>2</sub> layers labeled 1, 15, 17, 19, 21, and 23, which indicates ferromagnetic EuO does not affect the BTO/STO part. This absence of magnetism is similar to one reported Ref. [29].

Integrating the PDOS near the Fermi level, we estimate the 2DHG surface charge density in the BTO surface TiO<sub>2</sub> layer to be  $17.4 \mu\text{C}/\text{cm}^2$  ( $0.17e$  total charge) and the total charge at the BTO/STO interface is equal and opposite in sign. In Fig. 4(a) the black line shows the polarization of each BTO layer induced by Ti and O ions rumpling (the details of rumpling and its relation to polarization will be discussed later). Adding the average spontaneous polarization of the BTO layer ( $18.0 \mu\text{C}/\text{cm}^2$ ) and the depolarizing electric field induced by the 2DEG-2DHG in the opposite direction yields a net electric field in BTO of only  $0.06 \text{ V}/\text{\AA}$ . This agrees well with the value  $0.075 \text{ V}/\text{\AA}$ , computed from the average potential. Using the Poisson equation ( $\frac{dD}{dz} = \rho_f$ , where  $D$  is the electric displacement and  $\rho_f$  is the free charge density) near the BTO/STO interface, we can derive the discontinuity condition of displacement near the interface  $D_1 - D_2 = \sigma_f$  if we integrate across it; here  $D_1$  and  $D_2$  represent the electric displacements of the two components near the interface and  $\sigma_f$  is the interface free charge density. If we also assign the Ti displacement the dipole moment via Born effective charge, from Fig. 4(a), we find that the average polarization in STO is  $0.04 \text{ C}/\text{m}^2$  and the electric field is almost zero, which yields  $\sigma_f \approx 17.6 \mu\text{C}/\text{cm}^2$  near the BTO/STO interface, which

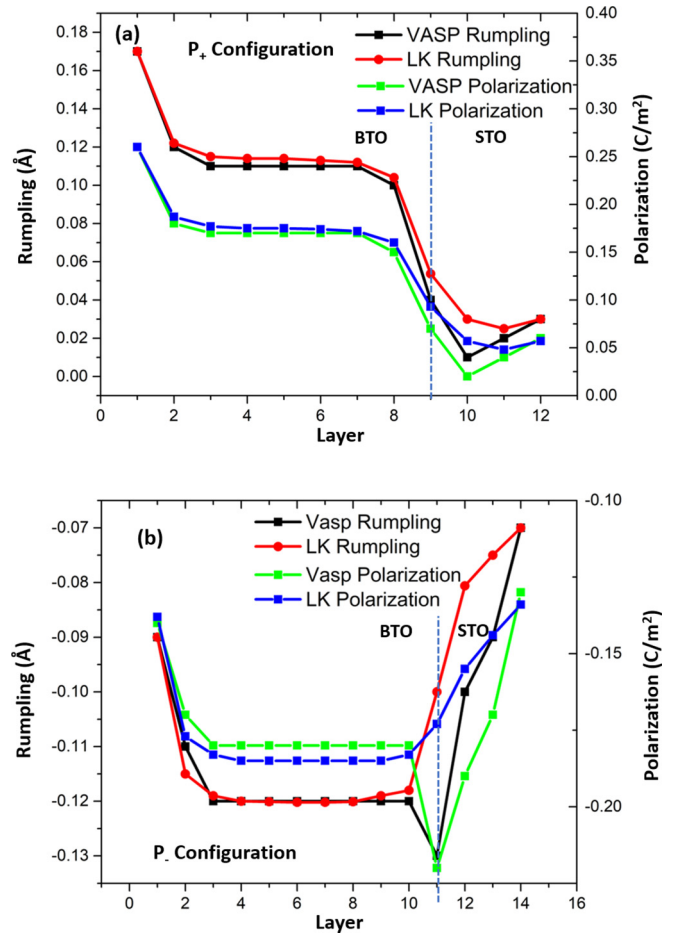


FIG. 4. (a), (b) Rumpling and polarization calculated from DFT and LK models are plotted for every layer (TiO<sub>2</sub> plane). The layer indices are according to the labels in Figs. 1(a) and 1(c). Blue dashed line indicates the mixed region TiO<sub>2</sub> plane.

agrees well with the PDOS integral. These results are in good agreement with Ref. [29].

In the configuration described by structure II, the polarization direction is reversed. Figure 5 shows the PDOS for each layer and AEP across the structure. From the AEP, we notice that the electric field in the BTO region now points towards the BTO/STO interface. However, the electric field inside the STO and EuO regions is overscreened and points in the opposite direction (see Supplemental Material Sec. I for details of the electronic structure [40]), as can also be seen in the PDOS. From the PDOS, we find a 100% spin-polarized 2DEG at the BTO surface and a 2DHG in the EuO region. To screen the polarization, electrons from the STO/EuO interface region transfer to BTO. Because the valence-band top of EuO (the “spin up”  $4f$  state) is  $\sim 1.5 \text{ eV}$  higher than the valence-band top of STO, the 2DHG is created on the EuO side of the interface. Because this is a purely spin-up band [Figs. 5(c) and 5(d)], both the 2DEG and 2DHG are 100% polarized and, consequently, the magnetization in EuO is reduced. Integrating the PDOS, we obtain the density of the 2DHG in the first EuO layer to be  $16.2 \mu\text{C}/\text{cm}^2$ , compared with the 2DHG value of  $52.64 \mu\text{C}/\text{cm}^2$  in EuO/Pt reported

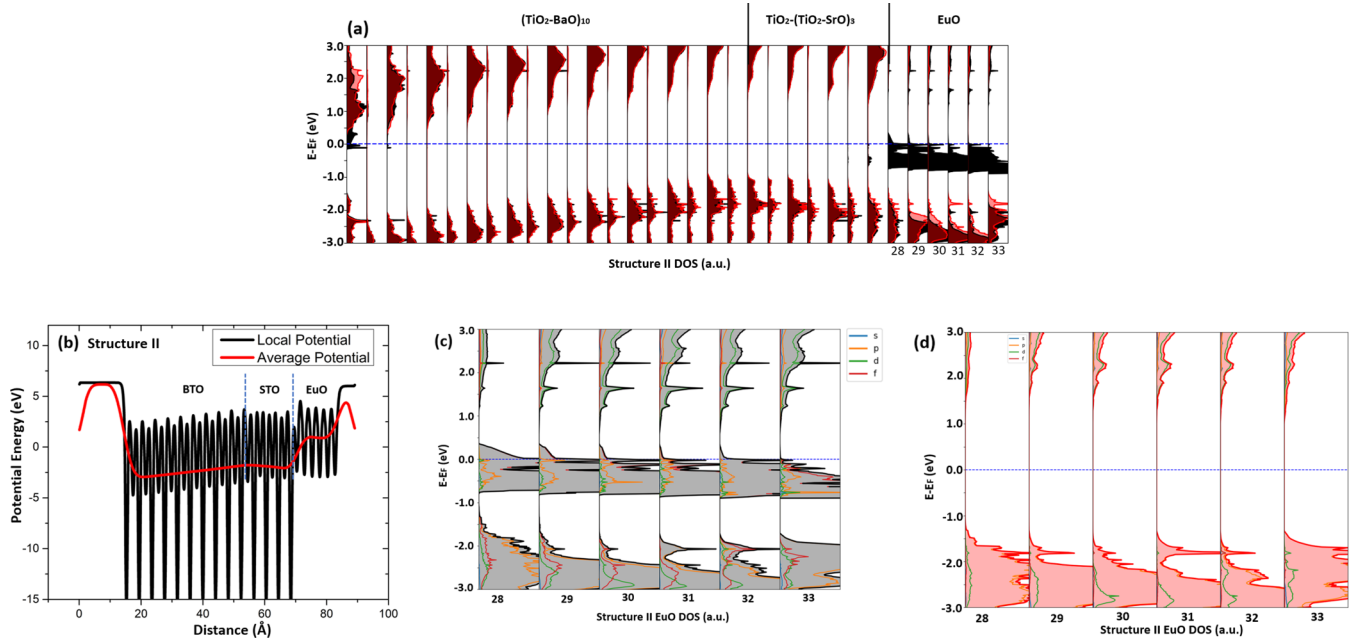


FIG. 5. (a) The PDOS analysis of structure II including both spin-up and -down channels. The color representation follows Fig. 3. The blue dashed line is the Fermi level. (b) The local electrostatic potential (black line) and macroscopically averaged potential (red line) are plotted along the simulation cell. The red line is calculated from Eq. (1). (c) PDOS analysis of the spin-up channel across six EuO layers. Color lines in the grey area show the orbital decomposition. (d) PDOS analysis of the spin down channel in six EuO layers. The legends of all color lines in the red area are the same as in (c).

by Ref. [36], as well as a hole carrier density of  $\sim 10^{22} \text{ cm}^{-3}$  in LAO/STO reported by Ref. [12].

### B. Field effect in the presence of oxygen vacancy

We now introduce an OV into structure I, and obtain structure III shown in Fig. 1(c). The lower-energy bonding state, formed by two  $|3d_{z^2} - p\rangle$  hybrid states localized on the two Ti atoms around the vacancy, lies in the gap of STO and traps one electron [9,11,41]. The second electron goes to the conduction band and then it can be shared across the heterostructure in accordance with the band alignment. In Fig. 6 we show the layer projected PDOS and AEP for structure III. We notice the in-gap state in STO, decaying in the first cell of EuO. Integrating the DOS in a narrow energy window around this in-gap state, we get one electron, which agrees well with Refs. [9,11,41]. Hence, the remaining electron moves inside the heterostructure. This means more free charge is available to screen the BTO polarization field. In addition, the in-gap state and 2DEG induced by the OV are spin polarized [15], and that can influence the magnetic properties of the 2DEG observed in structure I.

First, integrating the DOS in the 2DHG region at the BTO surface, we find the surface charge density to be  $5.4 \mu\text{C}/\text{cm}^2$  for the spin-up channel and  $7.4 \mu\text{C}/\text{cm}^2$  for the spin-down channel, resulting in a magnetic polarization  $p = 15.33\%$ . We also observe a highly spin polarized 2DEG in the BTO/STO interface region. In Figs. 7(a) and 7(b), we plot the PDOS of each EuO layer. In Fig. 7(a), we clearly see the Fermi level (blue dashed line) crossing the spin-up conduction band. This nearly 100% spin-polarized 2DEG spreads across the

entire EuO layer, suggesting that using the BTO ferroelectric polarization, one can indeed dope the EuO 5d band.

Comparing structures I and III, we conclude that, while the large portion of charge generated by the OV moves to the BTO/STO interface to screen the polarization [Figs. 7(c) and 7(d)], some fraction is doped into the EuO spin-up channel, as illustrated in Fig. 8. Based on the charge density analysis, the maximum number of doped electrons in EuO is approximately  $0.005e$  per Eu atom. This would increase the Curie temperature by  $\sim 10 \text{ K}$  [16,42], bringing it above liquid-nitrogen temperature. We would also like to point out that due to the GGA+ $U$  problem mentioned above, we freeze the ions in BTO, which overestimates the polarization. If the ferroelectric field is smaller, fewer electrons are needed to screen it and consequently, the carrier density in EuO could be larger and so would be the Curie temperature. Details about the orbital-decomposed DOS for the in-gap state and 2DEG are given in Supplemental Material Sec. II [40].

Second, the spin-polarized 2DEG aligns ferromagnetically with the EuO 4f states. The proximity effect of the Eu 4f state causes spin splitting of the Ti 3d states, producing spin polarization in STO. However, the in-gap vacancy state aligns antiferromagnetically with EuO, in contrast to the results of Ref. [15], where the in-gap state with ferromagnetic coupling was found to be more stable. The explanation is shown schematically in Fig. 9. As discussed in Refs. [9] and [43], the OV state is a magnetic impurity state and a spin singlet. Due to the polarization field, the spin-up electrons in the  $t_{2g}$  conduction band are driven to EuO, but the lowest empty band is the spin-up 5d band. As a result, the spin-down electrons are trapped by the in-gap state. The EuO conduction-band spin

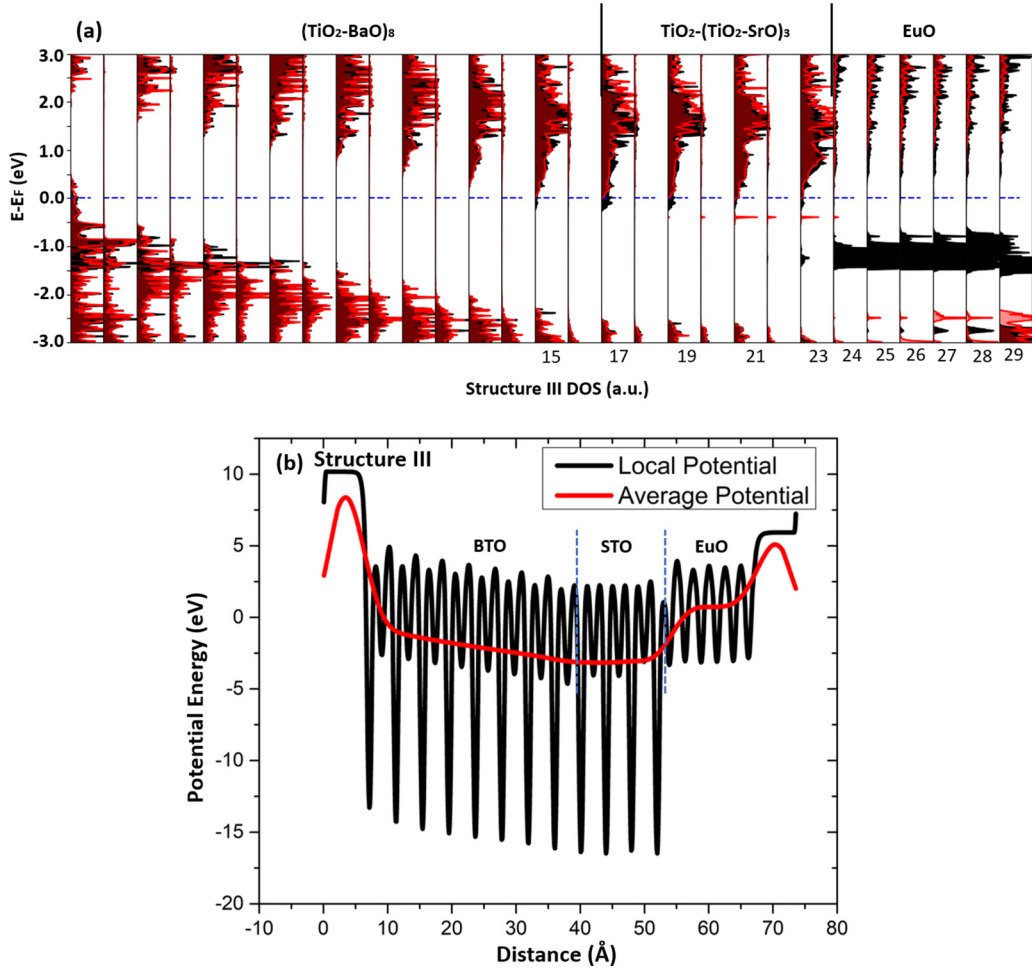


FIG. 6. (a) The PDOS analysis of structure III including both spin-up and -down channels. The color representation follows Fig. 3. (b) Local electrostatic potential (black line) and macroscopically averaged potential (red line) are plotted along the simulation cell. The red line is calculated from Eq. (1).

splitting is 0.6 eV, and ferromagnetic coupling is insufficient to overcome such a barrier. This can be thought of as a “remote” magnetoelectric coupling effect.

We introduce one OV to structure IV in the same position as structure III. Figure 10 shows the PDOS projected on each

layer and AEP for structure IV. Because we cannot observe any spin-polarized electron or hole doping in EuO, we will not discuss this case any further (details of the analysis are given in Supplemental Material Sec. III [40]). All our results discussed above are summarized in Table I.

TABLE I. Summary of the electronic structure calculation results. BTO-S stands for BTO surface, BTO/STO and STO/EuO stand for the corresponding interfaces, and BTO, STO, and EuO describe the bulk area of corresponding material.

Structure	Oxygen vacancy and simulation cell size	BTO polarization configuration	Carriers location	Carriers type	Max surface charge density ( $\mu\text{C}/\text{cm}^2$ ) observed	Spin polarization
I	no	$P_+$	BTO-S	2DHG	+17.4	0%
	$1\times 1$		BTO/STO	2DEG	−17.4	0%
II	No	$P_-$	BTO-S	2 DEG	−16.2	100%
	$1\times 1$		STO/EuO and EuO,	2DHG	+16.2	100%
III	yes	$P_+$	BTO-S	2DHG	Details in Fig. 8	
	$2\times 2$		BTO/STO and STO	2DEG		
			STO/EuO and EuO	2DEG		
IV	yes	$P_-$	Trivial case, not focused here			
	$2\times 2$					

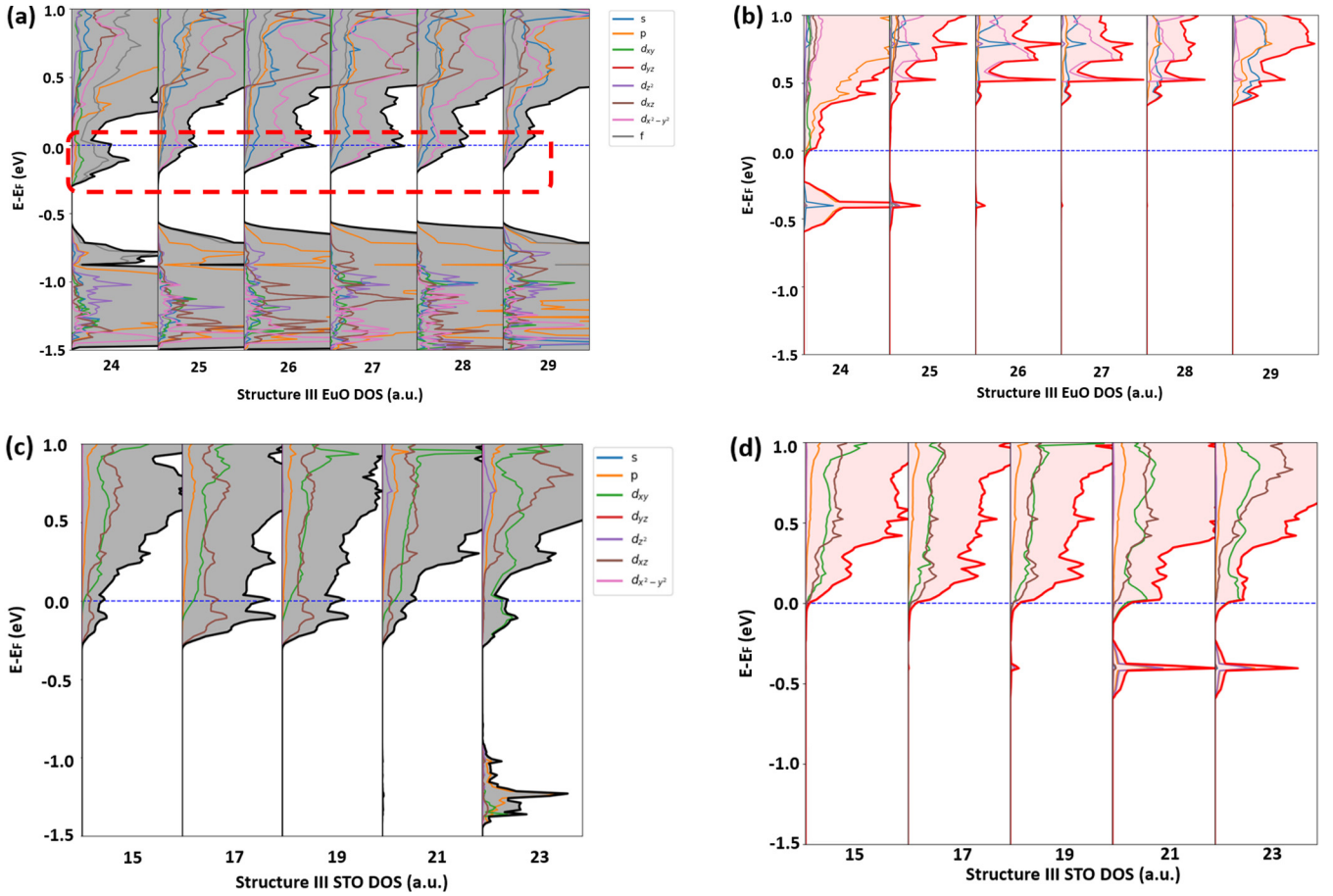


FIG. 7. (a) PDOS analysis of the spin-up channel in six EuO layers. Red dashed rectangular box highlights the 2DEG in EuO. Color lines in the grey area show the orbital decomposition. (b) PDOS analysis of the spin-down channel in six EuO layers. The legends of all color lines in the red area are the same as in (a). (c) PDOS analysis of the spin-up channel in  $\text{TiO}_2$  layers at the BTO/STO interface and in the STO bulk area. Color lines in the grey area show the orbital decomposition. (d) PDOS analysis of the spin-down channel in  $\text{TiO}_2$  layers. The legends of all color lines in the red area are the same as in (c).

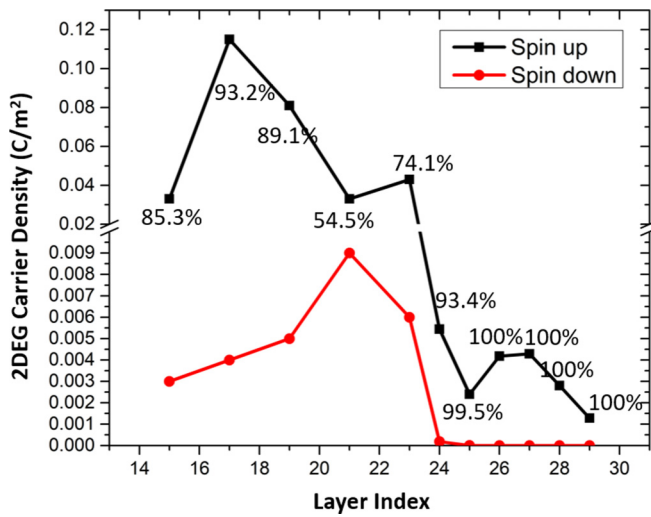


FIG. 8. Integrals of the PDOS yield the carrier density. We plot the carrier density for every layer where the 2DEG exists in STO and EuO. Black line shows charge density of the spin-up channel and red of the spin-down channel. The percentage near each data point is the spin polarization  $p$  calculated from  $p = \frac{n^\uparrow - n^\downarrow}{n^\uparrow + n^\downarrow}$ .

### C. Polarization profile: Landau-Khalatnikov model

The polarization in BTO and induced polarization in STO are the salient features of this heterostructure. We keep the polarization in BTO fixed, while the polarization in the STO layer is allowed to relax; as a result, STO acquires polarization in the same direction as ferroelectric BTO. A similar behavior of STO has been reported by Fredrickson and Demkov, who considered the BTO/STO interface [29]. Fundamentally, both the electrons and ions in STO can screen the external field. However, in titanates the lattice polarizability is much larger than the electronic one. This is true until the field is strong enough to induce dielectric breakdown (the 2DEG or 2DHG). Thus, for strong fields, there are two competing mechanisms of screening postbreakdown: electronic polarization and lattice polarization. Changes in one mechanism can influence the other one significantly. Since we want an accurate electronic structure description, we also need to make sure the polarization profile is reasonable. Thus, we shall now focus on the atomic structure related to the lattice polarization. We compare our first-principles results with the Landau-Khalatnikov (LK) model, which despite being mesoscopic in nature, gives very similar polarization values and reinforces our claim.



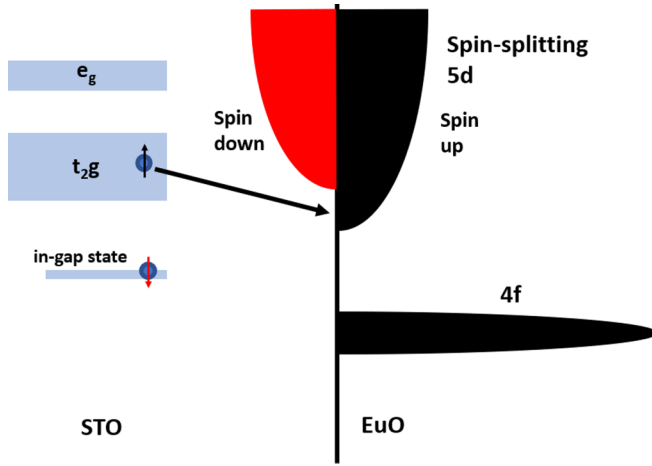


FIG. 9. Schematic of the magnetic character of the in-gap state. Blue, red, and black areas are the energy bands in STO and EuO. Black arrow represents spin-up charge-transfer direction.

The Landau-Khalatnikov model [38] describes the time-dependent relationship between the Landau free energy, electric field, and polarization:  $\mathbf{E} = \left(\frac{\partial F}{\partial \mathbf{P}}\right)_T + \rho \left(\frac{d\mathbf{P}}{dt}\right)$ , where  $\mathbf{E}$  is the external electric field,  $F$  is the Landau free energy,  $\mathbf{P}$  is

the polarization vector, and  $\rho$  is the resistivity. In the absence of an external electric field, the time-dependent equation is reduced to

$$\rho \left(\frac{d\mathbf{P}}{dt}\right) = - \left(\frac{\partial F}{\partial \mathbf{P}}\right)_T. \quad (2)$$

In the Ginsburg-Landau-Devonshire theory, the free energy can be expanded in powers of polarization  $\mathbf{P}$  as

$$F = \alpha_1 P^2 + \alpha_2 P^3 + \alpha_3 P^4 + \alpha_4 P^5 + \alpha_5 P^6 + \dots (\text{higher order terms}),$$

where  $\alpha_i$  are the expansion coefficients. For simplicity we will keep the expansion order to  $P^4$  and drop the odd order terms to get the free-energy expression:

$$F = \frac{\alpha}{2} P^2 + \frac{\beta}{4} P^4,$$

where  $\alpha$  and  $\beta$  are expansion coefficients with different values for BTO and STO, and ferroelectricity arises if  $\alpha < 0$ . Figure 11 shows a schematic of the BTO/STO heterostructure in the LK model, where the springs represent the nearest-neighbor coupling. Supplemental Material Sec. IV [40] provides further details of the BTO/STO free-energy model and polarization dynamics. It should be pointed out that this use of

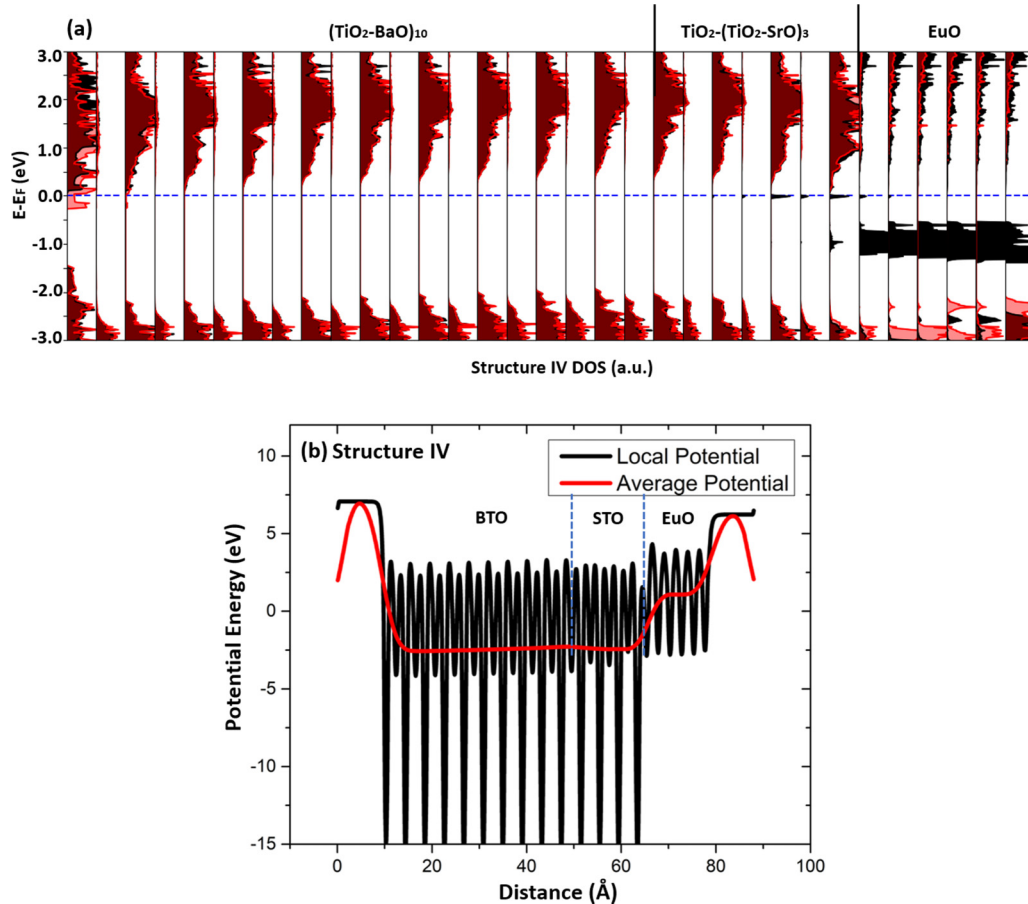


FIG. 10. (a) The PDOS analysis of structure IV including both spin-up and -down channels. The color representation follows that of Fig. 3. The blue dashed line is the Fermi level. (b) Local electrostatic potential (black line) and macroscopically averaged potential (red line) are plotted along the simulation cell. The red line is calculated from Eq. (1).

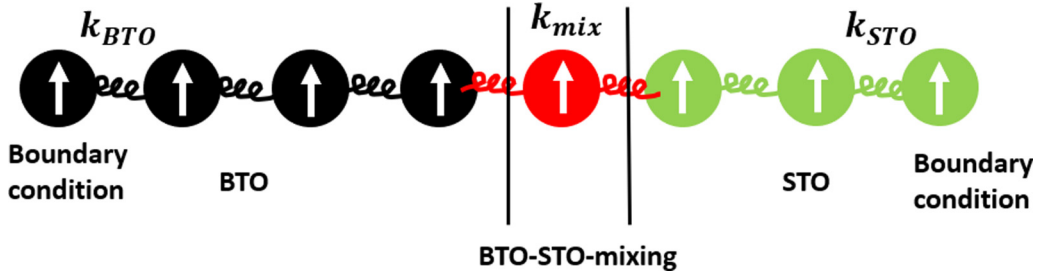


FIG. 11. Schematic of the Landau-Devonshire free energy model. Each black ball is one perovskite unit cell of BTO, green ball is a cell of STO, and red ball is the BTO-STO-mixed region. The white arrow inside each ball shows the polarization direction. Boundary conditions are set to match the DFT results.

the LK theory is clearly outside its intended length scale, as the theory is not microscopic. Still, it works surprisingly well.

The boundary conditions for the first and last  $\text{TiO}_2$  planes are chosen to match the DFT results. As for the initial conditions, we choose  $0.05 \text{ C/m}^2$  for the  $P_i$  configuration and  $-0.05 \text{ C/m}^2$  for the  $P_s$  configuration. For the expansion coefficients we use empirical values for BTO [44]  $\alpha_{\text{BTO}} = -1.13 \times 10^8 \text{ N m}^2/\text{C}^2$  and  $\beta_{\text{BTO}} = 3.68 \times 10^9 \text{ N m}^6/\text{C}^{-4}$  and  $\alpha_{\text{STO}} = 4.04 \times 10^8 \text{ N m}^2/\text{C}^2$  and  $\beta_{\text{STO}} = 6.80 \times 10^9 \text{ N m}^6/\text{C}^{-4}$  for STO [45].

We define the displacement as rumpling, or the distance between the Ti and O planes. Because the change of polarization is highly linear with respect to the change of displacement, to calculate polarization we use the approximation [46]

$$P_\beta = \frac{1}{\Omega} \sum_{\kappa} Z_{\kappa, \alpha\beta}^* \tau_{\kappa, \alpha}, \quad (5)$$

where  $\Omega$  is the volume of one perovskite unit cell,  $\kappa$  is the ion indices,  $\alpha$  and  $\beta$  are the Cartesian directions,  $\tau_{\kappa, \alpha}$  is the  $\kappa$  ion rumpling displacement along the  $\alpha$  direction,  $P_\beta$  is the polarization along  $\beta$ , and  $Z_{\kappa, \alpha\beta}^*$  is the Born effective charge tensor  $\alpha\beta$  component of ion  $\kappa$ . We assume that in a perovskite cell only the Ti ion moves along the  $z$  direction. Hence, Eq. (5) can be simplified to

$$P_z = \frac{1}{\Omega} Z_{\text{Ti}, zz}^* \tau_{\text{Ti}, z}. \quad (6)$$

Due to the inverse piezoelectric effect, STO between BTO and EuO experiences stress from the BTO field and its lattice constant in the  $z$  direction is influenced by the electric field across the simulation cell, so we use the strained volume ( $61.54 \text{ \AA}^3$  and  $61.52 \text{ \AA}^3$  for two STO cells). BTO is also strained and again we use the strained volume. After relaxation, the strained lattice constant in the  $z$  direction is  $4.11 \text{ \AA}$  in the bulklike region and the resultant volume is  $64.19 \text{ \AA}^3$ , 1.6% smaller when compared with the bulk value of  $65.26 \text{ \AA}^3$ . The Born effective charge is calculated as  $Z_{\kappa, \alpha\beta}^* = \Omega \frac{dP_\beta}{d\tau_{\kappa, \alpha}}$ , where we use  $Z_{\text{Ti}, zz}^*$  of  $6.17e$  in BTO and  $7.40e$  in STO [47–51]. To match the results of the DFT and LK models, we

choose  $k_{\text{BTO}} = 10^7 \text{ N m}^2/\text{C}^2$ , which results in a domain-wall thickness of  $3.46 \text{ \AA}$  in the BTO bulk region based on our microscopic length scale (calculation shown in Supplemental Material Sec. IV [40]) and  $k_{\text{STO}} = 10^9 \text{ N m}^2/\text{C}^2$ .

Because, in the presence of an OV, the displacements of Ti ions are complicated, we only use the LK model for structures I and III. The results are summarized in Fig. 4, where we compare the results of DFT and the phenomenological model. The relation between the rumpling and polarization is calculated using Eq. (6). The agreement is remarkably good.

#### IV. CONCLUSIONS

In summary, we investigate theoretically the effect of ferroelectric polarization on the magnetic properties of the 2DEG at the interface of an oxygen-deficient perovskite STO and EuO. To model this extrinsic magnetoelectric effect, we simulate four heterostructures of BTO/STO/EuO with different BTO polarization directions with and without an oxygen vacancy in STO. We predict 100% spin polarized doping in EuO, and a nearly 100% spin polarized 2DEG in the presence of oxygen vacancies in STO. In this case the field is driving electrons, introduced by an oxygen vacancy in STO, into the EuO spin-split  $5d$  conduction band. We also predict a 100% spin-polarized 2DHG in the EuO  $4f$  valence band for the oxygen vacancy-free heterostructure, when polarization is pointing away from the interface. To gain further insight into the polarization states of BTO and STO, as calculated within DFT, we numerically solve the two-component LK model and find remarkably good agreement. Our results suggest a way to manipulate the quantum state of a 2DEG and its location using extrinsic coupling of ferroelectricity and ferromagnetism, and a promising way of inducing and controlling multiferroic properties in complex oxide heterostructures.

#### ACKNOWLEDGMENT

We thank A. Posadas, W. Guo, and J. Lee for insightful discussions and critical reading of the manuscript. The work was supported by the Air Force Office of Scientific Research under Grant No. FA9550-18-1-0053.

[1] A. Ohtomo and H. Y. Hwang, *Nature (London)* **427**, 423 (2004).

[2] J. A. Bert, B. Kalisky, C. Bell, M. Kim, Y. Hikita, H. Y. Hwang, and K. A. Moler, *Nat. Phys.* **7**, 767 (2011).

- [3] J. Goniakowski, F. Finocchi, and C. Noguera, *Rep. Prog. Phys.* **71**, 016501 (2008).
- [4] H. Y. Hwang, *Science* **313**, 1895 (2006).
- [5] A. Kalabukhov, R. Gunnarsson, J. Börjesson, E. Olsson, T. Claeson, and D. Winkler, *Phys. Rev. B* **75**, 121404(R) (2007).
- [6] G. Herranz, M. Basletić, M. Bibes, C. Carrétéro, E. Tafr, E. Jacquet, K. Bouzehouane, C. Deranlot, A. Hamzić, J. M. Broto, A. Barthélémy, and A. Fert, *Phys. Rev. Lett.* **98**, 216803 (2007).
- [7] K. J. Kormondy, A. B. Posadas, T. Q. Ngo, S. Lu, N. Goble, J. Jordan-Sweet, X. Gao, D. J. Smith, M. R. McCartney, J. G. Ekerdt, and A. A. Demkov, *J. Appl. Phys.* **117**, 095303 (2015).
- [8] B. I. Edmondson, S. Liu, S. Lu, H. Wu, A. B. Posadas, D. J. Smith, X. Gao, A. A. Demkov, and J. G. Ekerdt, *J. Appl. Phys.* **124**, 185303 (2018).
- [9] C. Lin and A. A. Demkov, *Phys. Rev. Lett.* **111**, 217601 (2013).
- [10] K. J. Kormondy, L. Gao, X. Li, S. Lu, A. B. Posadas, S. Shen, M. Tsoi, M. R. McCartney, D. J. Smith, J. Zhou, L. L. Lev, M. Husanu, V. N. Strocov, and A. A. Demkov, *Sci. Rep.* **8**, 7721 (2018).
- [11] C. Mitra, C. Lin, J. Robertson, and A. A. Demkov, *Phys. Rev. B* **86**, 155105 (2012).
- [12] H. Lee, N. Campbell, J. Lee, T. J. Asel, T. R. Paudel, H. Zhou, J. W. Lee, B. Noesges, J. Seo, B. Park, L. J. Brillson, S. H. Oh, E. Y. Tsymbal, M. S. Rzchowski, and C. B. Eom, *Nat. Mater.* **17**, 231 (2018).
- [13] C. Chen, L. Fang, J. Zhang, G. Zhao, and W. Ren, *Sci. Rep.* **8**, 467 (2018).
- [14] B. R. K. Nanda and S. Satpathy, *Phys. Rev. Lett.* **101**, 127201 (2008).
- [15] L. Gao and A. A. Demkov, *Phys. Rev. B* **97**, 125305 (2018).
- [16] J. Lee, N. Sai, and A. A. Demkov, *Phys. Rev. B* **82**, 235305 (2010).
- [17] Y. Wang, M. K. Niranjana, J. D. Burton, J. M. An, K. D. Belashchenko, and E. Y. Tsymbal, *Phys. Rev. B* **79**, 212408 (2009).
- [18] P. V. Lukashev, A. L. Wysocki, J. P. Velez, M. van Schilfgaarde, S. S. Jaswal, K. D. Belashchenko, and E. Y. Tsymbal, *Phys. Rev. B* **85**, 224414 (2012).
- [19] P. Lömkert, T. C. Rödel, T. Gerber, F. Fortuna, E. Frantzeskakis, P. Le Fèvre, F. Bertran, M. Müller, and A. F. Santander-Syro, *Phys. Rev. Mater.* **1**, 062001 (2017).
- [20] S. Datta and B. Das, *Appl. Phys. Lett.* **56**, 665 (1990).
- [21] E. I. Rashba, *Phys. Rev. B* **62**, R16267 (2000).
- [22] G. Schmidt, D. Ferrand, L. W. Molenkamp, A. T. Filip, and B. J. van Wees, *Phys. Rev. B* **62**, R4790 (2000).
- [23] I. Žutić, J. Fabian, and S. D. Sarma, *Rev. Mod. Phys.* **76**, 323 (2004).
- [24] S. Sugahara, *Phys. Status Solidi C* **3**, 4405 (2007).
- [25] S. Sugahara and M. Tanaka, *Appl. Phys. Lett.* **84**, 2307 (2004).
- [26] Z. Gui and A. Janotti, *Phys. Rev. Lett.* **123**, 127201 (2019).
- [27] H. S. Lu, T. Y. Cai, S. Ju, and C. D. Gong, *Phys. Rev. Appl.* **3**, 034011 (2015).
- [28] D. Stornaiuolo, C. Cantoni, G. M. De Luca, R. Di Capua, E. Di Gennaro, G. Ghiringhelli, B. Jouault, D. Marré, D. Massarotti, F. M. Granozio, I. Pallecchi, C. Piamonteze, S. Rusponi, F. Tafuri, and M. Salluzzo, *Nat. Mater.* **15**, 278 (2015).
- [29] K. D. Fredrickson and A. A. Demkov, *Phys. Rev. B* **91**, 115126 (2015).
- [30] P. Ponath, K. D. Fredrickson, A. B. Posadas, Y. Ren, X. Wu, R. K. Vasudevan, M. B. Okatan, S. Jesse, T. Aoki, M. R. McCartney, D. J. Smith, S. V. Kalinin, K. Lai, and A. A. Demkov, *Nat. Commun.* **6**, 6067 (2015).
- [31] G. Kresse and J. Furthmüller, *Phys. Rev. B* **54**, 11169 (1996).
- [32] J. P. Perdew, K. Burke, and M. Ernzerhof, *Phys. Rev. Lett.* **77**, 3865 (1996).
- [33] P. E. Blöchl, *Phys. Rev. B* **50**, 17953 (1994).
- [34] C. Li, D. Cui, Y. Zhou, H. Lu, Z. Chen, D. Zhang, and F. Wu, *Appl. Surf. Sci.* **136**, 173 (1998).
- [35] R. E. Cohen, *Nature (London)* **358**, 136 (1992).
- [36] K. D. Fredrickson and A. A. Demkov, *J. Appl. Phys.* **119**, 095309 (2016).
- [37] W. Guo, A. B. Posadas, S. Lu, D. J. Smith, and A. A. Demkov, *J. Appl. Phys.* **124**, 235301 (2018).
- [38] L. D. Landau and I. M. Khalatnikov, *Dokl. Akad. Nauk SSSR* **96**, 469 (1954).
- [39] L. Kleinman, *Phys. Rev. B* **24**, 7412 (1981).
- [40] See Supplemental Material at <http://link.aps.org/supplemental/10.1103/PhysRevB.102.035308> for details.
- [41] C. Lin, C. Mitra, and A. A. Demkov, *Phys. Rev. B* **86**, 161102(R) (2012).
- [42] R. Sutarto, S. G. Altendorf, B. Coloru, M. Moretti Sala, T. Hauptrecht, C. F. Chang, Z. Hu, C. Schussler-Langeheine, N. Hollmann, H. Kierspel, J. A. Mydosh, H. H. Hsieh, H.-J. Lin, C. T. Chen, and L. H. Tjeng, *Phys. Rev. B* **80**, 085308 (2009).
- [43] G. Grosso and G. Parravicini, *Solid State Physics*, 2nd ed. (Elsevier, San Diego, 2013).
- [44] Y. Cho, P. Ponath, L. Zheng, B. Hatanpaa, K. Lai, A. A. Demkov, and M. C. Downer, *Appl. Phys. Lett.* **112**, 162901 (2018).
- [45] Q. Li, C. T. Nelson, S.-L. Hsu, A. R. Damodaran, L.-L. Li, A. K. Yadav, M. McCarter, L. W. Martin, R. Ramesh, and S. V. Kalinin, *Nat. Commun.* **8**, 1468 (2017).
- [46] R. Resta, M. Posternak, and A. Baldereschi, *Phys. Rev. Lett.* **70**, 1010 (1993).
- [47] S. H. Shah, P. D. Bristowe, A. M. Kolpak, and A. M. Rappe, *J. Mater. Sci.* **43**, 3750 (2008).
- [48] G. Catalan, J. F. Scott, A. Schilling, and J. M. Gregg, *J. Phys.: Condens. Matter* **19**, 022201 (2017).
- [49] V. A. Zhirnov, *Sov. Phys. JETP* **35**, 822 (1959).
- [50] G. Catalan, J. Seidel, R. Ramesh, and J. F. Scott, *Rev. Mod. Phys.* **84**, 119 (2012).
- [51] L. Shampine and M. Reichelt, *SIAM J. Sci. Comput.* **18**, 9 (1997).